

Diffusion-based smoothers for spatial filtering of gridded geophysical data

I. Grooms¹, N. Loose¹, R. Abernathey², J. M. Steinberg³, S. D. Bachman⁴, G.
Marques⁴, A. P. Guillaumin⁵, and E. Yankovsky⁵

¹Department of Applied Mathematics, University of Colorado, Boulder, Colorado, USA

²Lamont Doherty Earth Observatory of Columbia University, Palisades, New York, USA

³Woods Hole Oceanographic Institution, Woods Hole, Massachusetts, USA

⁴Climate and Global Dynamics Division, National Center for Atmospheric Research, Boulder, Colorado,

USA

⁵Courant Institute of Mathematical Sciences, New York University, New York, New York, USA

Key Points:

- A new way to apply a spatial low-pass filter to gridded data is developed
- The new method can be applied in any geometry since it only requires a discrete Laplacian operator
- The algorithm's flexibility is illustrated using a range of examples from simulation and observation data

Corresponding author: Ian Grooms, ian.grooms@colorado.edu

Abstract

We describe a new way to apply a spatial filter to gridded data from models or observations, focusing on low-pass filters. The new method is analogous to smoothing via diffusion, and its implementation requires only a discrete Laplacian operator appropriate to the data. The new method can approximate arbitrary filter shapes, including Gaussian and boxcar filters, and can be extended to spatially-varying and anisotropic filters. The new diffusion-based smoother’s properties are illustrated with examples from ocean model data and ocean observational products. An open-source python package implementing this algorithm, called `gcm-filters`, is currently under development.

Plain Language Summary

“The large scale part” and “the small scale part” of quantities like velocity, temperature, and pressure fluctuations are important for a range of questions in Earth system science. This paper describes a precise way of defining these quantities, as well as an efficient method for diagnosing them from gridded data, especially the data produced by Earth system models.

1 Introduction

Spatial scale is an organizing concept in Earth system science: atmospheric synoptic scales and convective scales, and oceanic mesoscales and submesoscales, for example, are ubiquitous touchstones in atmospheric and oceanic dynamics. The pervasive idea of an energy spectrum is fundamentally based on the idea of partitioning energy (or variance) across a range of spatial scales. Despite this central importance, diagnosing dynamics at different spatial scales remains challenging. When analysing remote-sensing or simulation data, scientists instead often rely on time averaging as proxy for separating scales, which is more computationally convenient than spatial filtering. Temporal filtering is often of interest in its own right, but in situations where spatial filtering is called for this trade of spatial for temporal filtering can be justified by the fact that dynamics at different spatial scales are frequently also associated with different time scales.

Spatial filtering has recently begun to replace time averages and zonal averages in *a priori* studies of subgrid-scale parameterization for ocean models. A canonical model for spatial filtering is given by kernel convolution

$$\bar{f}(\mathbf{x}) = \int_{\mathbb{R}^d} G(\mathbf{x} - \mathbf{x}')f(\mathbf{x}')d\mathbf{x}', \quad (1)$$

where G is the convolution kernel, \mathbf{x}' is a dummy integration variable, and \mathbb{R}^d denotes the set of all real vectors of length d . Berloff (2018), Bolton and Zanna (2019), Ryzhov et al. (2019), and Haigh et al. (2020) all used convolution filters to study subgrid-scale parameterization in the context of quasigeostrophic dynamics in a rectangular Cartesian domain. Lu et al. (2016), Aluie et al. (2018), Khani et al. (2019), Stanley, Bachman, and Grooms (2020), and Guillaumin and Zanna (2021) used approximate spatial convolutions on the sphere to filter ocean general circulation model output, and Aluie (2019) showed how to correctly define convolution on the sphere in such a way that the filter commutes with spatial derivatives. A ‘top hat’ or ‘boxcar’ kernel (i.e. an indicator function over a circle or a square, respectively) is used in all these studies, except for Bolton and Zanna (2019), Stanley, Bachman, and Grooms (2020), and Guillaumin and Zanna (2021) who used Gaussian kernels. Spatial convolution is not the only way to define or implement spatial filters. For example, Nadiga (2008) and Grooms et al. (2013) used an elliptic inversion to define spatial filters for quasigeostrophic model output, and Grooms and Kleiber (2019) used Fourier-based

63 filtering methods for primitive equation model output, all in rectangular Cartesian
64 domains.

65 We make a semantic distinction between spatial filtering and coarse graining. In
66 our use of the terms, coarse graining is an operation that produces output at a lower
67 resolution (i.e. smaller number of grid points) than the input, whereas spatial filtering
68 produces output at the same resolution as the input. (Note that this terminology
69 is not uniformly adopted in the literature; cf. Aluie et al. (2018).) Berloff (2005),
70 Porta Mana and Zanna (2014), Williams et al. (2016), Stanley, Grooms, et al. (2020),
71 and Zanna and Bolton (2020) are all examples where coarse graining was used in
72 the context of ocean model subgrid-scale parameterization. The term ‘averaging’ is
73 sometimes used instead of filtering. They are essentially synonymous when the filter
74 kernel G is non-negative, but a filter whose kernel has negative values cannot be
75 described as an average, so we opt to use the more general term. A low-pass filter can
76 be described as a smoother, which is the focus here, but the methods described here
77 can be straightforwardly adapted to band-pass or high-pass filters.

78 This paper introduces a new way of designing and implementing spatial filters
79 that relies only on a discrete Laplacian operator for the data. Because it relies on
80 the discrete Laplacian to smooth a field through an iterative process reminiscent of
81 diffusion, we refer to the new method as diffusion-based filters. The paper is structured
82 as follows. Section 2 describes the new filters along with their properties. Examples
83 using model data and observations are provided in section 3 to illustrate the various
84 filter properties described in section 2. Conclusions are offered in section 4.

85 2 Spatial filtering of gridded data

86 2.1 Review

87 Spatial filtering of gridded data is a well developed field, both for general appli-
88 cations and in the context of geophysical data. The focus here is on filtering in the
89 context of fluid models, especially atmosphere and ocean models. To place our new
90 method into context, we review existing filtering techniques, and distinguish between
91 implicit and explicit filters.

92 Shapiro (1970) introduced a class of filters, widely used to improve the perfor-
93 mance of early finite-difference weather models. Shapiro filters are essentially dis-
94 crete spatial convolution filters optimized to remove the smallest scales that can be
95 represented on a grid, while leaving the other scales as close to unchanged as pos-
96 sible. Sagaut and Grohens (1999) reviewed some of the more recent approaches to
97 convolution-based filtering for large-eddy simulation. Sadek and Aluie (2018) devel-
98 oped two discrete convolution kernels for the purpose of accurately extracting the
99 energy spectrum using convolution filters rather than Fourier methods.

Germano (1986) introduced an implicit differential filter of the form

$$(1 - L^2\Delta)\bar{f} = f, \tag{2}$$

100 where \bar{f} is the filtered field, L is the filter length scale, and Δ is the Laplacian. It is
101 ‘implicit’ because applying the filter to data involves solving a system of equations;
102 the convolution filters of Shapiro (1970) and Sagaut and Grohens (1999) are called ‘ex-
103 plicit’ in contrast. This is the kind of spatial filter used by Nadiga (2008) and Grooms
104 et al. (2013) in the context of subgrid-scale parameterization in quasigeostrophic ocean
105 models, and a similar fractional elliptic equation underlies the approach to spatial fil-
106 tering of scattered data recently developed by Robinson and Grooms (2020). Raymond
107 (1988) and Raymond and Garder (1991) developed implicit filters for meteorological
108 applications using higher order differential operators. Guedot et al. (2015) developed
109 higher order implicit differential filters on unstructured meshes for engineering appli-

110 cations. Note that the term ‘high order’ here refers to the differential operator, though
 111 it has been used elsewhere with different meanings (Sagaut & Grohens, 1999; Sadek
 112 & Aluie, 2018).

113 The new approach developed here results in high order explicit differential filters,
 114 meaning that they use a discrete Laplacian, but that they do not require solving a
 115 system of equations.

116 2.2 Spatial filtering basics

117 Most intuition about spatial filtering and spatial scales is built on the foundation
 118 of kernel convolution and Fourier analysis, in the context of equation (1). The well-
 119 known convolution theorem (e.g. Hunter & Nachtergaele, 2001, Theorem 11.35) states
 120 that the Fourier transform of \bar{f} is proportional to $\hat{G}\hat{f}$, where $\hat{\cdot}$ denotes the Fourier
 121 transform and the proportionality constant depends on the dimension d and on the
 122 normalization convention chosen in the definition of the Fourier transform.

123 Fourier analysis enables us to understand the effect of spatial convolution filtering
 124 in terms of length scales. We consider the function f to be a sum of many Fourier
 125 modes, each of which has a distinct spatial scale. The Fourier transform of the kernel,
 126 \hat{G} , then describes how each Fourier mode is modified by the spatial filtering operation.
 127 Filter kernels are usually symmetric about the origin, which makes \hat{G} real-valued, so
 128 that spatial filtering only changes the amplitude of the Fourier modes and not their
 129 phase. If $\hat{G}(k) = 1$ for a particular Fourier mode then the corresponding length scale
 130 is left unchanged in f , whereas if $\hat{G}(k) = 0$ for a particular Fourier mode then the
 131 corresponding length scale is removed from f . By modifying the amplitudes of the
 132 Fourier modes, spatial filtering controls the scale content of f .

One of the simplest kernels is the so-called boxcar function, defined in one spatial
 dimension as

$$G_L(x) = \begin{cases} 1/L & |x| < L/2 \\ 0 & |x| > L/2 \end{cases} \quad (3)$$

133 This represents averaging all the points in the neighborhood with the same weight,
 134 and the parameter L defines the size of the neighborhood. (In higher dimensions the
 135 boxcar filter is nonzero over a square region, while a ‘top-hat’ filter is nonzero over a
 136 circular or spherical region.) The Fourier transform of the boxcar filter of width L is

$$\hat{G}_L(k) = \text{sinc}\left(\frac{kL}{2\pi}\right) \quad (4)$$

137 where $\text{sinc}(x) = \sin(\pi x)/(\pi x)$ and k is the wavenumber. This function decays only
 138 as $1/k$ at large k , so it does not correspond to a sharp separation between length
 139 scales. Conversely, a ‘spectral truncation’ filter has a kernel whose Fourier transform
 140 is a boxcar, and the kernel itself is a sinc function. The boxcar and spectral truncation
 141 filters illustrate the concept that a short-range kernel does not separate scales well,
 142 and a filter that makes a sharp separation between scales requires a very long-range
 143 kernel. Figure 1 shows the boxcar and sinc convolution kernels, to illustrate that
 144 the more scale-selective sinc kernel has a much longer range. In practice there is a
 145 tradeoff between choosing a kernel that makes as clean a scale separation as possible
 146 and choosing a kernel whose range is short enough to apply efficiently.

147 It is usually desirable for the filter to preserve the integral, and to commute with
 148 derivatives, i.e.

$$\int_{\mathbb{R}^d} f(\mathbf{x})d\mathbf{x} = \int_{\mathbb{R}^d} \bar{f}(\mathbf{x})d\mathbf{x}, \quad (5)$$

$$\frac{\partial \bar{f}}{\partial x_i} = \frac{\partial f}{\partial x_i}. \quad (6)$$

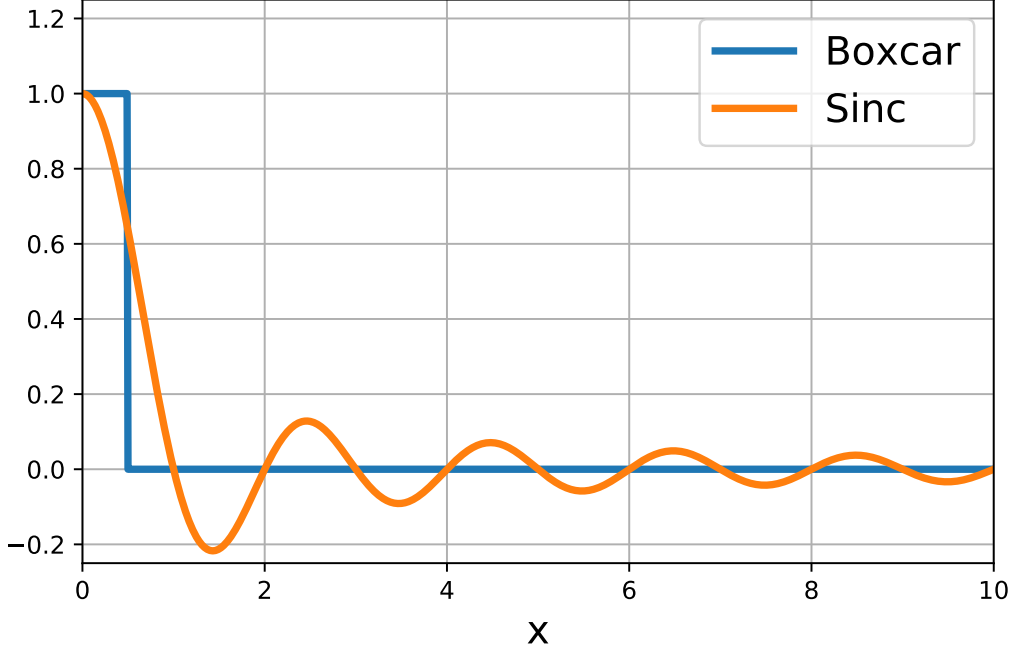


Figure 1. The boxcar function of width 1 and $\text{sinc}(x)$.

149 Any convolution filter commutes with derivatives, and preservation of the integral is
 150 easily ensured by the condition

$$\int_{\mathbb{R}^d} G(\mathbf{x})d\mathbf{x} = 1. \quad (7)$$

151 In the presence of boundaries the convolution formula (1) no longer works, since $f(\mathbf{x})$
 152 is not defined on \mathbb{R}^d . One option, used by Aluie et al. (2018), is to simply set $f(\mathbf{x}) = 0$
 153 outside the domain boundaries. The more common option is to vary the kernel near
 154 the boundaries so that the filter formula changes to

$$\bar{f}(\mathbf{x}) = \int_{\Omega} G(\mathbf{x}, \mathbf{x}')f(\mathbf{x}')d\mathbf{x}', \quad (8)$$

155 where $\Omega \subset \mathbb{R}^d$ is the spatial domain and \mathbf{x}' is a dummy integration variable. This kind
 156 of spatial filter no longer commutes with spatial derivatives, though it still preserves
 157 the integral as long as the kernel is appropriately normalized.

158 The background intuition for kernel-based spatial filters in this subsection is
 159 developed entirely for functions on Euclidean spaces. The definition of convolution-
 160 based spatial filters is considerably more complicated on a sphere; see Aluie (2019) for
 161 details.

162 **2.3 Diffusion-based smoothers**

163 **2.3.1 Discrete integral & Laplacian**

164 To generalize the foregoing ideas to more complicated domains and grid geometries
 165 we begin with a transition to the discrete representation. The field to be filtered
 166 is no longer a continuous function, but a vector \mathbf{f} ; for example, if we wish to filter
 167 temperature on a grid of n points, then we think of the values of temperature on the

168 grid as a vector in \mathbb{R}^n . To lay a foundation for the analysis we need two ingredients;
 169 the first is a discrete integral

$$\int_{\Omega} f(\mathbf{x})d\mathbf{x} \approx \sum_i w_i f_i, \quad (9)$$

170 where Ω denotes the spatial domain and w_i are positive weights. Cartesian geometry is
 171 assumed for ease of presentation, but the discrete integral could easily approximate an
 172 integral over the sphere or some other smooth manifold without changing the analysis.
 173 For a typical finite-volume model the weight w_i will simply be the area (or volume, if
 174 the integral is over three spatial dimensions) of the i^{th} grid cell. If the weights w_i are
 175 all positive then we can define a discrete inner product

$$\langle \mathbf{f}, \mathbf{g} \rangle = \sum_i w_i f_i g_i. \quad (10)$$

176 The area integral can be expressed in terms of the inner product as $\langle \mathbf{1}, \mathbf{f} \rangle$, where $\mathbf{1}$ is
 177 a vector whose entries are all 1.

178 The second ingredient is a discrete Laplacian, i.e. some operation on \mathbf{f} that
 179 produces an approximation of Δf on the grid. We write this operation in matrix
 180 form as $\mathbf{L}\mathbf{f}$, though it is certainly not necessary to actually construct the matrix \mathbf{L} .
 181 We assume that the discrete Laplacian is negative semi-definite, and self-adjoint with
 182 respect to the discrete inner product, i.e for any \mathbf{f} and \mathbf{g}

$$\langle \mathbf{f}, \mathbf{L}\mathbf{f} \rangle \leq 0, \text{ and } \langle \mathbf{f}, \mathbf{L}\mathbf{g} \rangle = \langle \mathbf{L}\mathbf{f}, \mathbf{g} \rangle. \quad (11)$$

183 This is automatically guaranteed for finite-volume discretizations of the Laplacian with
 184 no-flux boundary conditions.

185 *2.3.2 Connecting the discrete Laplacian to spatial scales*

186 Since the discrete Laplacian is self-adjoint and negative semi-definite, the eigen-
 187 values of \mathbf{L} are all real and non-positive, and there is an eigenvector basis $\mathbf{q}_1, \dots, \mathbf{q}_n$
 188 of \mathbb{R}^n that is orthonormal with respect to the discrete inner product. This is directly
 189 analogous to the Fourier analysis of the foregoing section: Fourier modes on \mathbb{R}^d are
 190 eigenfunctions of the Laplacian on \mathbb{R}^d . In fact, with an equispaced grid and periodic
 191 boundaries the eigenvectors \mathbf{q}_i are exactly the discrete Fourier modes. In both the
 192 Fourier version and the discrete version the eigenvalues can be interpreted as describ-
 193 ing the spatial scale of the corresponding eigenfunction:

$$\Delta e^{i\mathbf{k}\cdot\mathbf{x}} = -k^2 e^{i\mathbf{k}\cdot\mathbf{x}}, \quad \mathbf{L}\mathbf{q}_i = -k_i^2 \mathbf{q}_i. \quad (12)$$

194 On the left in the above expression $k = \|\mathbf{k}\|$ represents the familiar Fourier wavenumber
 195 corresponding to a wavelength of $2\pi/k$, while on the right the eigenvalue $-k_i^2$ has
 196 been written with similar notation to emphasize the similarity. Precisely because \mathbf{L} is
 197 a discretization of the Laplacian, the length $2\pi/k_i$ should roughly correspond to the
 198 length scale of the eigenvector \mathbf{q}_i .

199 Continuing the analogy with the previous section, it is possible to write the vector
 200 to be filtered as a sum over eigenfunctions of the discrete Laplacian:

$$\mathbf{f} = \sum_{i=1}^n \hat{f}_i \mathbf{q}_i. \quad (13)$$

201 We next show that we can filter \mathbf{f} by applying a function $p(-\mathbf{L})$ to it. From equation
 202 (13), we see that this results in

$$p(-\mathbf{L})\mathbf{f} = \sum_{i=1}^n \hat{f}_i p(k_i^2) \mathbf{q}_i = \sum_{i=1}^n \hat{f}_i \hat{G}(k_i) \mathbf{q}_i, \quad (14)$$

203 where the notation $\hat{G}(k) = p(k^2)$ has been deliberately used to emphasize the connec-
 204 tion to the Fourier convolution theorem recalled in the previous section: if the expansion
 205 coefficients of \mathbf{f} are \hat{f}_i , then the expansion coefficients of $p(-\mathbf{L})\mathbf{f}$ are $\hat{G}(k_i)\hat{f}_i$. (The
 206 notation p is used for both the matrix and scalar versions of the function; a familiar
 207 example might be $p(-\mathbf{L}t) = e^{-\mathbf{L}t}$ and $p(0) = e^0 = 1$.) If one defined the function p in
 208 such a way that

$$\hat{G}(k) = \begin{cases} 1 & k < k_* \\ 0 & k \geq k_* \end{cases}, \quad (15)$$

209 then multiplying \mathbf{f} by $p(-\mathbf{L})$ would correspond to projecting \mathbf{f} onto large-scale modes
 210 defined by $k_i < k_*$. This would be analogous to a spectral truncation filter. Since the
 211 discrete filter is a function of a discrete Laplacian, it is natural to suspect that the
 212 filter should commute with derivatives; this question is addressed in Appendix B.

213 **2.3.3 Polynomial approximation of the target filter**

214 For the large data sets produced by Earth system models computing the eigen-
 215 values and eigenvectors of \mathbf{L} is prohibitively expensive, and even solving linear systems
 216 involving \mathbf{L} can be expensive. By contrast, simply applying \mathbf{L} is usually inexpensive.
 217 In practice this means that it is inexpensive to compute $p(-\mathbf{L})\mathbf{f}$ when p is a poly-
 218 nomial. (The implicit differential filters of Germano (1986) and Guedot et al. (2015)
 219 correspond to letting $1/p$ be a polynomial.)

220 We propose to define our new filters as $\bar{\mathbf{f}} = p(-\mathbf{L})\mathbf{f}$, where p is a polynomial

$$p(-\mathbf{L}) = a_0\mathbf{I} + a_1(-\mathbf{L}) + \dots + a_N(-\mathbf{L})^N. \quad (16)$$

221 The polynomial coefficients a_i will be chosen as described below to obtain the desired
 222 filter shape, and \mathbf{I} is the identity matrix. To show that such a filter preserves the
 223 integral, note that $p(-\mathbf{L})$ is self-adjoint with respect to the discrete inner product,
 224 and

$$\langle \mathbf{1}, \bar{\mathbf{f}} \rangle = \langle \mathbf{1}, p(-\mathbf{L})\mathbf{f} \rangle = \langle p(-\mathbf{L})\mathbf{1}, \mathbf{f} \rangle = \langle a_0\mathbf{1}, \mathbf{f} \rangle, \quad (17)$$

225 where we have used the fact that $\mathbf{L}\mathbf{1} = \mathbf{0}$ for any consistent discretization of the Lapla-
 226 cian with no-flux boundary conditions. The condition $a_0 = p(0) = 1$ thus guarantees
 227 that the spatial filter will preserve the integral. It also ensures that the filter will leave
 228 large scales approximately unchanged; in order to remove small scales p should decay
 229 towards zero as k increases.

230 We can choose a specific shape for p by means of standard polynomial approx-
 231 imation of a ‘target’ filter \hat{G}_t . For example, note that the Fourier transform of a
 232 Gaussian convolution kernel with standard deviation L is

$$\hat{G}(k) = \exp\left\{-\frac{L^2 k^2}{2}\right\}. \quad (18)$$

233 In order to construct a filter that acts like a convolution-based spatial filter with a
 234 Gaussian kernel of standard deviation L , one might choose a target filter of the form
 235 $\hat{G}_t(k) = \hat{G}(k)$.

236 The goal would then be to find a polynomial p such that $p(k^2) \approx \hat{G}_t(k)$. In
 237 general this is not possible with an explicit filter because polynomials grow without
 238 bound as $k \rightarrow \pm\infty$; thankfully it is only necessary for the approximation to hold over
 239 the range of scales represented on the grid, specifically for $0 \leq k \leq k_n$ where $-k_n^2$
 240 is the most-negative eigenvalue of \mathbf{L} . If k_n is not known, some reasonable proxy can
 241 be used to define the range of scales over which p should act like a spatial filter. For
 242 example, on a quadrilateral grid one might use $0 \leq k \leq \sqrt{d}\pi/dx_{\min}$ where dx_{\min} is
 243 the length of the smallest grid cell edge and d is the spatial dimension of the grid.

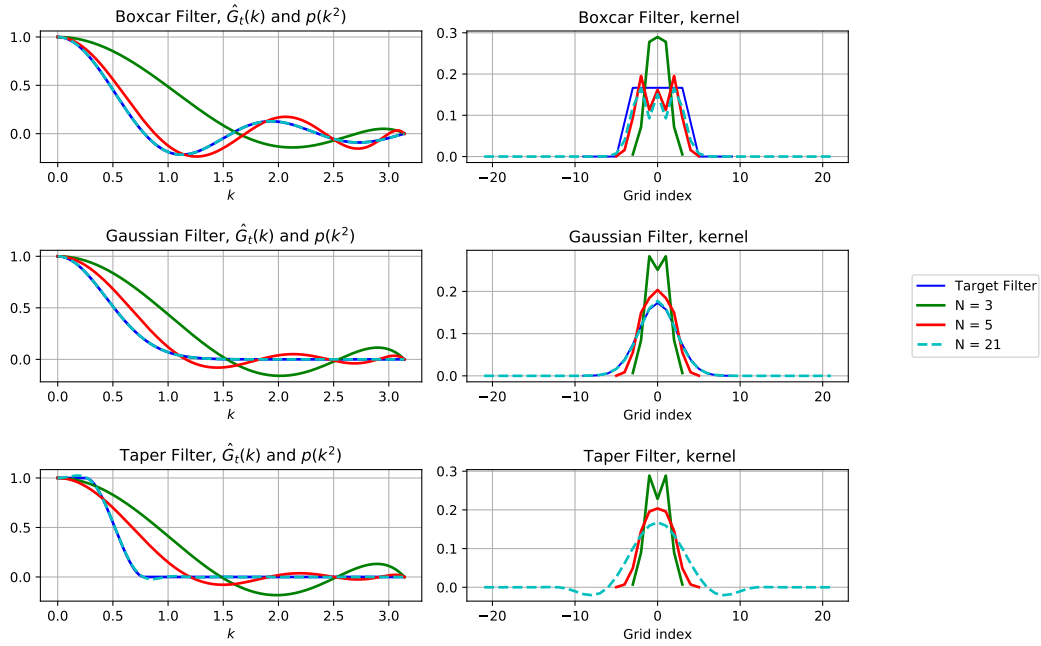


Figure 2. Left: Target filters $\hat{G}_t(k)$ and their approximations $p(k^2)$. Right: The equivalent kernel weights in one dimension on an equispaced grid of size 1. Top Row: A boxcar filter of width 8; Middle Row: A Gaussian filter with standard deviation $4/\sqrt{3}$; Bottom Row: The taper filter. All length scales in this figure are nondimensional. There is no blue line in the lower right panel because the taper filter is defined directly in terms of its target $\hat{G}_t(k)$, rather than via its convolution kernel, as for the boxcar and Gaussian filters.

244 In Appendix A we present a least-squares approach for finding a polynomial p
 245 such that $p(k^2)$ approximates $\hat{G}_t(k)$. The left column of Figure 2 shows three examples
 246 of target filters, along with their approximations $p(k^2)$ using polynomials of degree
 247 $N = 3, 5,$ and 21 . The top row shows the boxcar target shown in equation (4) with
 248 length scale $L = 8$ (nondimensional), and the middle row shows the Gaussian target
 249 that corresponds to a Gaussian kernel with standard deviation $4/\sqrt{3}$ (nondimensional).
 250 The bottom row shows a target that we here label ‘taper.’

251 The taper target is a piecewise polynomial with a continuous first derivative. It
 252 is $\hat{G}_t(k) = 0$ for k above some cutoff $k_c = 2\pi/L$, with $L = 8$ (nondimensional) in
 253 Figure 2. For $0 \leq k \leq k_c/X$ it takes the value $\hat{G}_t(k) = 1$ where X controls the width
 254 of the transition region; $X = \pi$ in Figure 2. For wavenumbers in the transition region
 255 $k_c/X \leq k \leq k_c$ the taper target is a cubic polynomial. As the width of the transition
 256 region goes to zero ($X \rightarrow 1$) the taper target approaches the spectral truncation filter,
 257 which is a step function at wavenumber k_c . The left column of Figure 2 shows that
 258 the number of steps N required to achieve an accurate approximation of the target
 259 filter depends on the shape of the target filter, with more scale-selective targets like
 260 the taper requiring more steps N .

261 2.3.4 Definition of filter scale

262 We provide a single definition of the ‘filter scale’ for the boxcar, Gaussian, and
 263 taper targets as follows. The filter scale for a boxcar kernel is simply the width of
 264 the kernel L (not the half-width). Per equation (4), the boxcar filter exactly zeros out
 265 the wavenumber $k = 2\pi/L$. Since the taper filter also zeros out wavenumber $2\pi/L$, it
 266 is natural to let L define the ‘filter scale’ for both the boxcar and taper filters. The
 267 filter scale for a Gaussian is chosen so that the standard deviation of the Gaussian and
 268 boxcar kernels match for a given filter scale (cf. Sagaut & Grohens, 1999). This is
 269 achieved by defining the ‘filter scale’ L for a Gaussian to be $\sqrt{12}$ times the standard
 270 deviation of the Gaussian kernel, i.e. to extract the standard deviation σ from the
 271 filter scale L use $\sigma = L/(2\sqrt{3})$.

272 2.3.5 Filter algorithm

273 Once the approximating polynomial has been found, the filtered field $p(-\mathbf{L})\mathbf{f}$ can
 274 be efficiently computed using an iterative algorithm based on the polynomial roots. In
 275 general, any polynomial with real coefficients has roots that are either real, or come
 276 in complex-conjugate pairs. We can thus write

$$p(s) = a_N(s - s_1) \cdots (s - s_M)(s^2 - 2sR\{s_{M+2}\} + |s_{M+2}|^2) \cdots (s^2 - 2sR\{s_N\} + |s_N|^2), \quad (19)$$

277 where M is the number of real roots, the roots are s_1, \dots, s_N , and $R\{\cdot\}$ and $I\{\cdot\}$
 278 denote the real and imaginary parts of a complex number, respectively. The quadratic
 279 terms can also be written $|s - s_k|^2 = (s - R\{s_{M+2}\})^2 + (I\{s_{M+2}\})^2$. The condition
 280 $p(0) = 1$ implies

$$p(s) = \left(1 - \frac{s}{s_1}\right) \cdots \left(1 - \frac{s}{s_M}\right) \left(1 + \frac{-2sR\{s_{M+2}\} + s^2}{|s_{M+2}|^2}\right) \cdots \left(1 + \frac{-2sR\{s_N\} + s^2}{|s_N|^2}\right). \quad (20)$$

281 Based on this representation, the filtered field $\bar{\mathbf{f}} = p(-\mathbf{L})\mathbf{f}$ can be computed in $M +$
 282 $(N - M)/2$ stages as follows. First the real roots are dealt with via

$$\bar{\mathbf{f}} = \mathbf{f} \quad (21a)$$

$$\bar{\mathbf{f}} \leftarrow \bar{\mathbf{f}} + \frac{1}{s_k} \mathbf{L}\bar{\mathbf{f}}, \quad k = 1, \dots, M. \quad (21b)$$

283 These stages are called Laplacian stages. Next the complex roots are dealt with via

$$\bar{\mathbf{f}} \leftarrow \bar{\mathbf{f}} + \frac{2R\{s_k\}}{|s_k|^2} \mathbf{L}\bar{\mathbf{f}} + \frac{1}{|s_k|^2} \mathbf{L}^2\bar{\mathbf{f}}, \quad k = M + 2, M + 4, \dots, N. \quad (22)$$

284 These stages are called biharmonic stages because of the need to apply the discrete
 285 biharmonic operator \mathbf{L}^2 .

286 In the absence of roundoff errors the Laplacian and biharmonic stages can be ap-
 287 plied in any order, and once they are both complete $\bar{\mathbf{f}}$ contains the filtered field (though
 288 at any point in the middle of the iterations $\bar{\mathbf{f}}$ has no particular meaning). However, in
 289 practice the order can have an impact on numerical stability. This issue is discussed
 290 in the following subsection. The form of equation (21b) is directly reminiscent of time
 291 integration of the diffusion equation via an explicit Euler discretization, and in some
 292 sense the method can be thought of as smoothing through diffusion.

293 2.4 Numerical Stability

294 Recall that per equation (13) we can formally expand the field to be filtered as a
 295 sum of eigenvectors of the discrete Laplacian, and that per equation (14) the effect of
 296 the filter is simply to modify the coefficients in this expansion. The same idea applies
 297 to a single stage in the iterative application of the filter. A single Laplacian stage
 298 multiplies the expansion coefficients by

$$1 - \frac{k_i^2}{s_k}. \quad (23)$$

299 Any modes i such that $k_i^2 > 2s_k$ will have their coefficients \hat{f}_i amplified at this stage,
 300 and smaller scales will experience greater amplification. (The sign of the coefficients
 301 will also be changed; the real roots s_k are generally positive.) In contrast, when
 302 $|1 - k_i^2/s_k| < 1$ none of the modes will experience amplification and the smallest scales
 303 will be damped.

304 A single biharmonic stage multiplies the expansion coefficients by

$$\left| 1 - \frac{k_i^2}{s_k} \right|^2. \quad (24)$$

305 As a function of k_i this is a positive parabola that equals 1 at $k_i = 0$. When the real
 306 part of s_k is negative all modes are amplified with increasing amplification at small
 307 scales. When the real part of s_k is positive, modes with $k_i^2 > 2\mathcal{R}\{s_k\}$ will be amplified,
 308 with increasing amplification at small scales.

309 A filter that attempts to remove a wide range of scales, i.e. one where the filter
 310 scale is much larger than the grid scale, will have many small values of s_k that corre-
 311 spond to stages where the small scales are amplified, and will also have many stages
 312 overall since it requires more stages to accomplish more smoothing. If there are several
 313 stages in succession that cause amplification at the small scales, it can lead to extreme
 314 amplification at small scales, including extreme amplification of any roundoff errors
 315 present in the small scales. This combination of many amplifying stages, together
 316 with a large number of stages for roundoff errors to accumulate, can lead to inaccurate
 317 results or even blowup of the filtered field. To avoid this we recommend choosing a
 318 specific order for the roots s_k , such that stages that amplify small scales are always
 319 followed by stages that damp small scales.

320 To illustrate these ideas we set up a simple toy problem with a one-dimensional,
 321 periodic, equispaced grid of 256 points in a nondimensional domain of size 2π , and a
 322 spectral discrete Laplacian. The eigenvectors of the discrete Laplacian are the discrete
 323 Fourier modes with wavenumbers $k = -127, \dots, 128$, and the eigenvalues are exactly
 324 $-k^2$. The filter polynomial p is constructed by directly specifying the roots s_k , rather
 325 than by approximating some target filter \hat{G}_t . The roots s_k are the integers from 43 to
 326 170, squared (i.e. there are $N = 128$ stages). This filter should thus exactly zero out
 327 all discrete wavenumbers with $|k| \geq 43$, while smoothly damping wavenumbers with

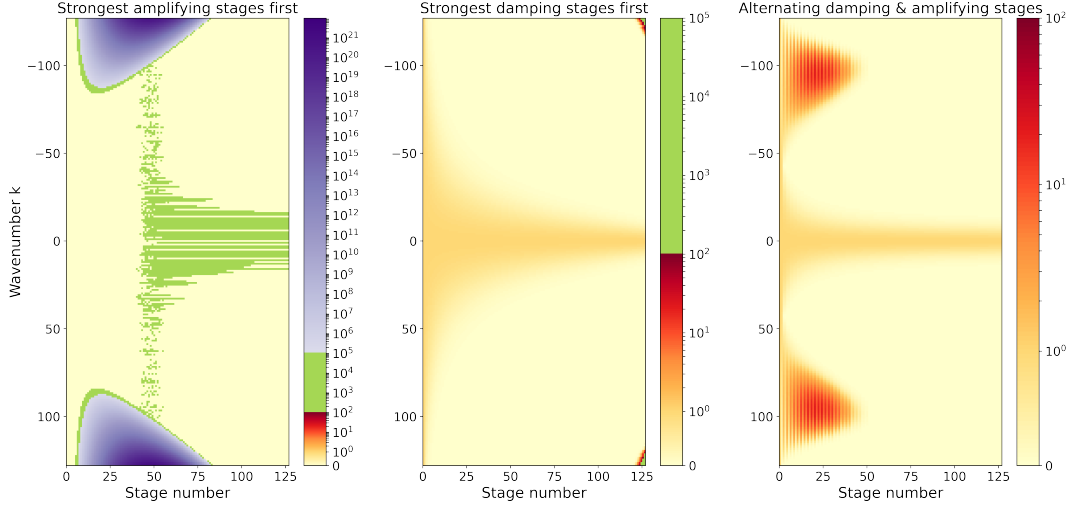


Figure 3. Amplitude of the Fourier coefficients of $\bar{\mathbf{f}}$ as it proceeds through the filter stages. In each panel the abscissa is filter stage while the ordinate is the wavenumber. In the left panel s_k are arranged in increasing order. In the center panel the s_k are decreasing. In the right panel the damping and amplifying stages alternate.

328 $|k| < 43$. The field to be filtered is constructed to have discrete Fourier transform
 329 $\hat{f}_k = e^{i\theta_k}$ where θ_k are independent and uniformly distributed on $[0, 2\pi)$. This initial
 330 condition is chosen so that the discrete Fourier transform of the final filtered field
 331 should, in the absence of roundoff errors, have absolute value equal to $|p(k^2)|$.

332 Figure 3 shows the amplitude of the Fourier modes of the field as it progresses
 333 through the stages of the filter. The left panel shows the result for a filter where s_k are
 334 ordered from least to greatest, such that the first stages amplify the small scales while
 335 the last stages damp them. The small scales grow to amplitudes on the order of 10^{21}
 336 within the first 50 stages. The subsequent stages manage to damp these small scales
 337 back out, but the solution is so corrupted by the effect of roundoff errors that the final
 338 solution is completely inaccurate: the large scales have amplitudes on the order of 10^4 .

339 The center panel of Figure 3 shows the effect of arranging s_k in decreasing order,
 340 such that the last stages amplify the small scales while the first stages damp them. The
 341 filter behaves quite well until the final few stages, where the small scales are amplified
 342 to the order of 10^4 . Evidently the initial damping stages introduce small amplitude
 343 roundoff errors into the small scales which are then amplified in the final stages.

344 The right panel of Figure 3 shows the effect of arranging the s_k so that the small
 345 scales are alternately amplified and then damped. In the early stages of the filter there
 346 is a range of intermediate scales that begins to amplify, though they maintain modest
 347 amplitudes less than 100. These intermediate scales are eventually damped back out
 348 in the later stages, leading to a well-behaved and accurate solution.

349 The stages in the right panel of Figure 3 are arranged in the following simple
 350 way. We first compute the impact of each stage on the smallest scale, given by setting
 351 $k_i = k_{\max}$ in the absolute value of expression (23) and in expression (24). These values
 352 are then ordered, and the stage order is set by selecting the smallest value (strongest
 353 damping) first, followed by the largest value (strongest amplification), followed by the
 354 next-smallest value, etc.

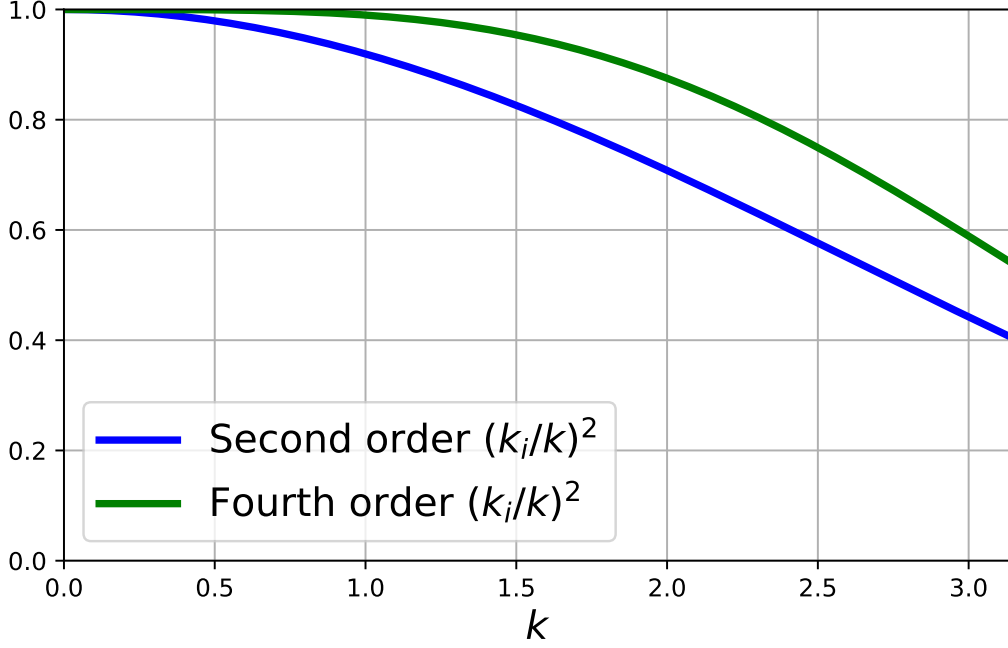


Figure 4. The ratio of the eigenvalues $-k_i^2$ of the discrete Laplacians to the true value $-k^2$. The second-order Laplacian is shown in blue and the fourth-order Laplacian is shown in green.

355

2.5 Impact of the order of accuracy of the discrete Laplacian

356

357

358

359

360

361

362

363

This section gives a simple example to show that higher-order discretizations of the Laplacian should be better able to sharply distinguish between scales near the grid scale. The fundamental idea of section 2.3 is that the eigenvalues of the discrete Laplacian correspond to the spatial length scale of the eigenvector in the same way that this correspondence works for the continuous Fourier problem, i.e. if $-k_i^2$ is an eigenvalue of the discrete Laplacian then the length scale of the corresponding eigenvector \mathbf{q}_i is assumed to be $2\pi/k_i$. This connection between eigenvalues and length scales can be inaccurate at small length scales.

364

365

For example, consider the following two discrete Laplacians on an infinite or periodic one-dimensional equispaced grid with grid spacing 1 (nondimensional)

$$(\mathbf{L}_2\mathbf{f})_j = f_{j-1} - 2f_j + f_{j+1} \quad (25)$$

$$(\mathbf{L}_4\mathbf{f})_j = -\frac{1}{12}f_{j-2} + \frac{4}{3}f_{j-1} - \frac{5}{2}f_j + \frac{4}{3}f_{j+1} - \frac{1}{12}f_{j+2}. \quad (26)$$

366

For both of these Laplacians the discrete Fourier modes

$$(\mathbf{q}_k)_j = e^{ikj} \quad (27)$$

367

368

369

370

are eigenvectors, where $0 \leq k \leq \pi$ is the discrete wavenumber, \mathbf{L}_2 is second order, and \mathbf{L}_4 is fourth order. (Note that notation has been changed from \mathbf{q}_i in section 2.3 to \mathbf{q}_k here, so that k is the discrete wavenumber rather than i .) For a spectral discretization the eigenvalues would be $-k^2$, but the eigenvalues for the second and fourth order

371 Laplacians are

$$\mathbf{L}_2 \mathbf{q}_k = -4 \sin^2 \left(\frac{k}{2} \right) \mathbf{q}_k \quad (28)$$

$$\mathbf{L}_4 \mathbf{q}_k = -\frac{2}{3} (7 - \cos(k)) \sin^2 \left(\frac{k}{2} \right) \mathbf{q}_k. \quad (29)$$

372 The fact that these are not equal to $-k^2$ is tantamount to saying that the filter will
 373 incorrectly identify the length scales of the eigenfunctions. Figure 4 shows the ratio
 374 of the discrete eigenvalues (28) and (29) to the correct value $-k^2$. In both cases
 375 the wavenumber implied by the eigenvalue is smaller than the true wavenumber k ,
 376 meaning that these Laplacians treat small scales as if they were larger-scale than they
 377 really are. Both Laplacians have accurate eigenvalues at large scales, but the fourth
 378 order Laplacian's eigenvalues are more accurate at small scales. A filter that uses the
 379 fourth order Laplacian will thus be more accurate when the filter is attempting to
 380 separate scales near the limit of resolution. If one is attempting, for example, to get
 381 an accurate estimate of the energy spectrum at scales near the grid scale using the
 382 diffusion-based filter of section 2.3 in combination with the method of Sadek and Aluie
 383 (2018) for estimating the spectrum, then it would be important to use a high-order
 384 discretization of the Laplacian. On the other hand, if the filter is attempting to remove
 385 the entire range of small scales where the second-order Laplacian is inaccurate, then
 386 the second order Laplacian will work as well as higher-order Laplacians.

387 2.6 Spatially varying filter properties

388 The filters developed in section 2.3 are based on the isotropic Laplacian, and are
 389 therefore isotropic in the sense that they provide an equal amount of smoothing in every
 390 direction. The filter coefficients are the same over the whole domain, so the degree of
 391 smoothing is also constant over the domain. This can be generalized to anisotropic
 392 and spatially-varying filters by letting \mathbf{L} be a discretization of $\nabla \cdot \mathbf{K}(\mathbf{x}) \nabla$ where $\mathbf{K}(\mathbf{x})$
 393 is a symmetric and positive definite tensor that varies in space (cf. Báez Vidal et al.,
 394 2016). (In this context \mathbf{K} is nondimensional, since the dimensions are carried by the
 395 polynomial roots s_i .)

396 Consider first the isotropic case $\mathbf{K} = \kappa \mathbf{I}$ with constant κ , and assume that the
 397 filter polynomial $p(k^2)$ has been designed as described in section 2.3 under the as-
 398 sumption $\kappa = 1$. If the filter polynomial is used with constant $\kappa \neq 1$ then the filter
 399 polynomial $p(k^2)$ is replaced by $p(\kappa k^2)$. This is tantamount to rescaling the filter
 400 length scale by $\sqrt{\kappa}$. For example, if the original filter with $\kappa = 1$ had a characteristic
 401 length scale of L then the filter using $\kappa \neq 1$ has a characteristic length scale of $\sqrt{\kappa}L$.

402 Next consider the case of an isotropic Laplacian with spatially-varying κ , and
 403 assume that κ varies slowly over the domain. The filter polynomial p is designed to
 404 have length scale L if $\kappa = 1$. In regions where $\kappa > 1$ the filter will have a longer length
 405 scale $\sqrt{\kappa}L$, while in regions where $\kappa < 1$ the filter will have a smaller length scale. (If
 406 κ varies on length scales smaller than the filter scale then the behavior of the filter is
 407 hard to predict, so this situation should be avoided.)

408 Finally, consider the case of an anisotropic Laplacian with symmetric and posi-
 409 tive definite \mathbf{K} that varies over the domain. At each point in the domain \mathbf{K} has
 410 two orthogonal eigenvectors corresponding to different directions, and the eigenvalues
 411 indicate the strength of smoothing in each direction. One natural application of the
 412 anisotropic Laplacian is to apply a filter whose length scale is tied to the local grid scale,
 413 which is especially relevant for Earth system models whose grid cell sizes vary in space.
 414 This can be achieved by aligning the eigenvectors of \mathbf{K} with the local orthogonal grid
 415 directions, and letting the respective eigenvalues determine the amount of filtering in
 416 each direction.

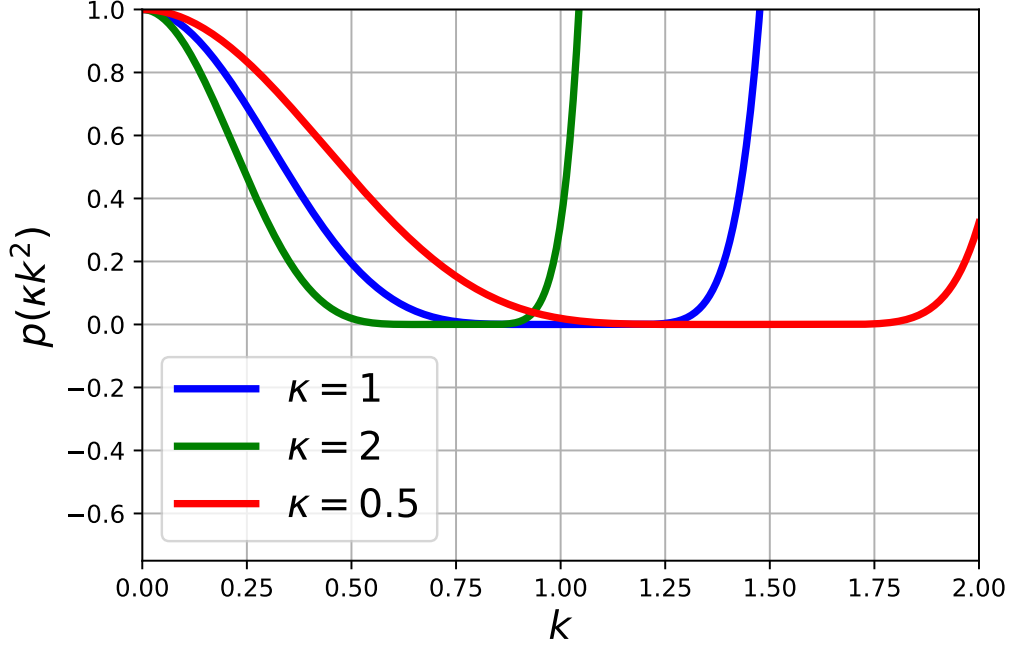


Figure 5. The effect of changing κ on the filter polynomial $p(\kappa k^2)$ for the polynomial p from equation (30).

417 A major caveat to the above discussion is that values of $\kappa > 1$ can lead to
 418 unexpected behavior. Consider, for example, the filter polynomial

$$p(\kappa k^2) = (1 - 0.7\kappa k^2)(1 - 0.8\kappa k^2) \cdots (1 - 1.2\kappa k^2), \quad (30)$$

419 where the scales that can be represented on the grid are associated with wavenumbers
 420 $0 \leq k \leq 1$ and the standard case uses $\kappa = 1$. The blue line in Figure 5 shows that
 421 $p(k^2)$ only acts as a smoother over the range of scales associated with $0 \leq k \leq 1$; at
 422 larger k that are not represented on the grid the filter will significantly amplify these
 423 scales. Using $\kappa > 1$ has the effect of bringing this undesirable filter behavior into the
 424 range of scales represented on the grid, as can be seen in the green line corresponding
 425 to $\kappa = 2$ in Figure 5. In contrast, using $\kappa \leq 1$ has no such problems (blue and red in
 426 Figure 5). It is thus desirable to specify $\kappa \leq 1$ whenever possible.

427 Consider, for example, a one-dimensional non-uniform grid with maximum grid
 428 spacing h_{\max} , minimum grid spacing h_{\min} , and local grid spacing h . To apply a filter
 429 that smooths locally to a scale m times larger than the local grid, one could choose
 430 the filter scale to be $L = mh_{\min}$ and then set $\kappa = (h/h_{\min})^2$. Locally the filter scale
 431 is rescaled to $\sqrt{\kappa}L = (h/h_{\min})(mh_{\min}) = mh$ as desired, but at the same time $\kappa \geq 1$
 432 which will lead to undesirable behavior at the small scales. Instead, one can achieve the
 433 same effect by setting the filter scale to $L = mh_{\max}$, and then setting $\kappa = (h/h_{\max})^2$.
 434 The local filter scale is again $L = mh$, but with $\kappa \leq 1$ over the whole domain.

435 We next describe a more *ad hoc* method of tying the local filter scale to the local
 436 grid scale. This method is not without drawbacks, but it is simpler and faster than the
 437 method based on an anisotropic and spatially-varying Laplacian. We call this filter
 438 the simple fixed factor filter.

439 Let \mathbf{L}_0 be the discretization of the Laplacian if all the cells had the same size.
 440 Since the cell sizes are assumed equal, the matrix \mathbf{L}_0 should be symmetric. If we
 441 simply replaced $p(-\mathbf{L})$ by $p(-\mathbf{L}_0)$ in the definition of the filter it would imply that we
 442 were filtering *as if* all the grid cells were the same size, which is equivalent to making
 443 the scale of the filter relative to the scale of the local grid. Unfortunately this would
 444 no longer preserve the integral. To rectify this problem we propose a cell-size weighted
 445 filter, which amounts to the following recipe:

- 446 • Weight the input data by cell sizes
- 447 • Apply the filter assuming the cell sizes are equal
- 448 • Divide the result by the cell sizes.

449 We next show that this filter preserves the integral at the discrete level. First
 450 note that weighting by the cell size is equivalent to multiplication by a diagonal matrix
 451 \mathbf{W} whose diagonal entries are the cell sizes, so the above filter corresponds to

$$\bar{\mathbf{f}} = \mathbf{W}^{-1}p(-\mathbf{L}_0)\mathbf{W}\mathbf{f}. \quad (31)$$

452 The inner product (10) can be written in the form $\langle \mathbf{f}, \mathbf{g} \rangle = \mathbf{f}^T \mathbf{W} \mathbf{g}$, and recall that the
 453 discrete integral is $\langle \mathbf{1}, \mathbf{f} \rangle$. To prove that the new filter conserves the integral we follow
 454 (17), and find that

$$\langle \mathbf{1}, \bar{\mathbf{f}} \rangle = \mathbf{1}^T \mathbf{W} \mathbf{W}^{-1} p(-\mathbf{L}_0) \mathbf{W} \mathbf{f} = p(0) \mathbf{1}^T \mathbf{W} \mathbf{f} = \langle \mathbf{1}, \mathbf{f} \rangle. \quad (32)$$

455 The above sequence uses the facts that \mathbf{L}_0 is symmetric, which implies $\mathbf{1}^T \mathbf{L}_0 = (\mathbf{L}_0 \mathbf{1})^T$,
 456 that any consistent discretization of the Laplacian with no-flux boundary conditions
 457 will have $\mathbf{L}_0 \mathbf{1} = \mathbf{0}$, and that $p(0) = 1$.

458 Applying the discrete Laplacian under the assumption that all cell sizes are equal
 459 is much simpler than using an anisotropic Laplacian, and the algorithm can thus be
 460 much faster. On the other hand, this ad hoc method no longer has the property that
 461 the constant vector is left unchanged by the filter. Note that the simple fixed factor
 462 filter is anisotropic whenever the grid spacing is anisotropic, and it is spatially-varying
 463 whenever the grid spacing is non-uniform.

464 2.7 Variance reduction

465 In some situations it is desirable to enforce that the filtered field has less total
 466 variance than the unfiltered field, i.e. for functions

$$\int_{\Omega} f(\mathbf{x})^2 d\mathbf{x} \geq \int_{\Omega} \bar{f}(\mathbf{x})^2 d\mathbf{x} \quad (33)$$

467 and for the discrete case

$$\langle \mathbf{f}, \mathbf{f} \rangle \geq \langle \bar{\mathbf{f}}, \bar{\mathbf{f}} \rangle. \quad (34)$$

468 To translate this into a condition on the diffusion-based smoothers developed here,
 469 expand \mathbf{f} in the orthonormal basis of eigenvectors of \mathbf{L}

$$\mathbf{f} = \sum_{i=1}^n \hat{f}_i \mathbf{q}_i. \quad (35)$$

470 The condition of variance reduction becomes

$$\sum_{i=1}^n \hat{f}_i^2 \geq \sum_{i=1}^n \hat{f}_i^2 (p(k_i^2))^2. \quad (36)$$

471 In order for this to be satisfied for any possible vector \mathbf{f} this requires $|p(k_i^2)| \leq 1$ for
 472 every k_i up to the largest one represented on the model grid, i.e. k_n . The eigenvalues

473 $-k_i^2$ of the discrete Laplacian are usually not known exactly, so a sufficient condition for
 474 variance reduction would be that $|p(k^2)| \leq 1$ for every $0 \leq k \leq k_{\max}$ where $k_{\max} \geq k_n$.
 475 It is worth noting that this condition applies to p and not to the target filter. Even if
 476 the target filter satisfies this condition, the polynomial p might not satisfy it. (In all
 477 examples in the left column of Figure 2 both the target filter and the approximating
 478 polynomials do satisfy this condition.) It is also worth noting that failure to satisfy
 479 this condition does not guarantee that the filtered field has more total variance than
 480 the unfiltered field, but only that it might happen in some cases.

481 2.8 The effective kernel implied by the diffusion-based filter

482 If the spatial filter were defined by a discrete approximation of a kernel-based
 483 spatial filter (8) then the value of \bar{f} at the i^{th} grid cell would be

$$\bar{f}_i = \langle \mathbf{g}_i, \mathbf{f} \rangle = \sum_j w_j g_{ij} f_j, \quad (37)$$

484 where \mathbf{g}_i is the effective filter kernel corresponding to the i^{th} cell. Note that $\bar{f}_i =$
 485 $\langle \mathbf{e}_i, \bar{\mathbf{f}} \rangle / w_i$, where \mathbf{e}_i is a vector of zeros with 1 at the i^{th} grid cell. Next note that

$$\bar{f}_i = \frac{1}{w_i} \langle \mathbf{e}_i, p(-\mathbf{L})\mathbf{f} \rangle = \frac{1}{w_i} \langle p(-\mathbf{L})\mathbf{e}_i, \mathbf{f} \rangle, \quad (38)$$

486 which implies that $\mathbf{g}_i = p(-\mathbf{L})\mathbf{e}_i / w_i$. We can thus compute the effective filter kernel
 487 that corresponds to $p(-\mathbf{L})$ at the i^{th} grid cell by applying the filter to \mathbf{e}_i and then
 488 dividing the result by w_i . The same arguments can be used to find the effective filter
 489 kernel associated with the spatially-varying filters of section 2.6.

490 Note that if the filter kernel ever takes a negative value, then it is no longer
 491 guaranteed to preserve positivity in the sense that \mathbf{f} may have negative values even
 492 when all the values in \mathbf{f} are positive. The spectral truncation filter is such an example
 493 having negative weights.

494 The right column of Figure 2 computes the filter kernels associated with the
 495 polynomial approximations of the boxcar, Gaussian, and taper filters in the left column
 496 of Figure 2. The standard equispaced, second-order Laplacian (25) was used, with
 497 a nondimensional grid size of 1. The upper right panel illustrates that the kernel
 498 associated with the polynomial approximation of the boxcar filter does not converge
 499 to the actual boxcar kernel, though it is close. One reason for this discrepancy is the
 500 fact that the boxcar target (4) was formulated by reference to a continuous Fourier
 501 transform, which is not a one-to-one match to the discrete version. Another reason
 502 is that the effective kernel depends on the discretization of the Laplacian; a higher-
 503 order discretization would result in a slightly different effective kernel. Despite these
 504 discrepancies, the effective kernel of the polynomial approximation to a Gaussian target
 505 still converges to a close approximation of the expected Gaussian kernel, as can be seen
 506 in the middle right panel of Figure 2.

507 3 Illustrative Examples

508 In this section we present examples using model output and observational data to
 509 illustrate the various filter properties and capabilities. An open-source python package
 510 implementing the diffusion-based filters described in section 2, called gcm-filters, is cur-
 511 rently under development and will be described elsewhere. This Python code includes
 512 implementations of the discrete Laplacian on a variety of grids for different ocean gen-
 513 eral circulation models. All examples that show the filtering of two-dimensional data
 514 use a second-order discrete Laplacian (on a 5-point stencil) with no-flux boundary
 515 condition.

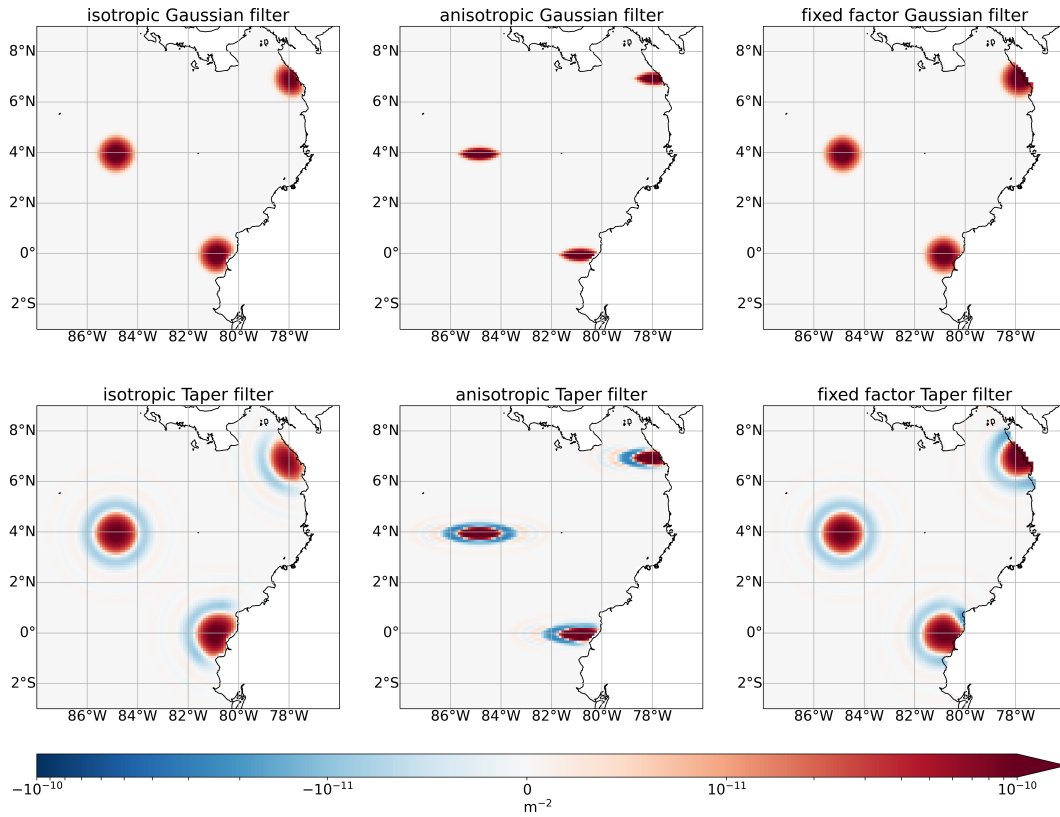


Figure 6. Effective filter kernels for six different filters on the 0.1 degree POP tripole grid, centered at 3 points in the equatorial Pacific. Top row: Gaussian; Bottom row: Taper. Left column: The isotropic version of the filter with a fixed filter scale of 111.7 km. Center column: The anisotropic version of the filters in the left column, but with a length scale 10 times smaller in the meridional direction. Right column: The simple fixed factor filter from Section 2.6, with filter scale equal to 10 times the local grid scale.

516

3.1 Effective Kernels

517

518

519

520

521

522

523

524

525

526

527

528

529

We begin with an example showing effective filter kernels (see section 2.8) for various configurations of the filters, noting especially how the filter kernel adapts near boundaries. Figure 6 shows the effective kernels for six different filter configurations, each at three locations in the equatorial Pacific Ocean. The grid is the 0.1 degree nominal resolution tripole grid of the Parallel Ocean Program (POP; Smith et al., 2010). The top row shows filters with a Gaussian target, while the bottom row shows filters with the taper target. It is clear that the taper target produces kernels with negative weights, while the Gaussian target does not. The left column corresponds to isotropic filters with a fixed length scale of 111.7 km, corresponding to 1 degree of latitude. The center column corresponds to anisotropic filters that are the same as the left column except that the filter scale has been decreased by a factor of 10 in the meridional direction. The right column corresponds to the simple fixed factor filter from Section 2.6, where we chose a filter scale of 10 times the local grid scale.

530

531

532

533

534

535

536

537

538

539

540

541

542

543

Since the grid is nominally 0.1 degree, the width of the fixed factor filter kernels in the right column is approximately equal to the width of the fixed scale filter kernels in the first column. Despite the similarity of the effective filter kernels in the first versus third columns, the computational effort of their underlying filters varies significantly: while the fixed scale Gaussian (Taper) filter in the first column requires $N = 90$ ($N = 319$) stages to achieve an approximation of the target filter with error less than 1%, the fixed factor versions in the third column need only $N = 18$ ($N = 64$) stages. This is explained by the fact that, by construction, the fixed scale filter has to remove a wider range of scales than the simple fixed factor filter, because the smallest grid spacing, dx_{\min} , of the POP grid is 2.2km. As a result, the filter with fixed scale $L = 111.7$ km has to remove scales up to 50 times the local grid scale, while the simple fixed factor filter removes only scales up to 10 times the local grid scale. The discrepancy in the number of necessary filter stages is reflected in the computational cost of the two filters.

544

3.2 Spatially varying filter scale

545

546

547

548

549

550

551

552

553

554

555

556

557

558

Figure 7 illustrates the ability of our filters to vary their length scales over the domain by using variable κ as described in Section 2.6. We filter the vertical component of relative vorticity at the surface from the submesoscale-resolving MITgcm simulation of the Scotia Sea described in Bachman et al. (2017). In the map of the unfiltered vorticity (top panel) large scales are evident in the Antarctic Circumpolar Current to the east of Drake Passage, where the first baroclinic deformation radius tends to be $O(10)$ km and is generally smaller than the eddies themselves. Small scales are ubiquitous over the continental shelf off the eastern coast of Argentina, where the deformation radius is $O(1)$ km and is much closer to the eddy scale. We demonstrate the spatially-varying filter by choosing the filter length scale so that the filter scale is proportional to the local first baroclinic deformation radius. In making this choice we expect that more features will be filtered out in the areas where the dynamics tend to be larger than the deformation scale, as shown in the map of the filtered vorticity (middle panel) and the difference, i.e. the eddy vorticity field (lower panel).

559

3.3 Non-commutation of the filter and spatial derivatives

560

561

562

563

564

565

Figure 8 illustrates the lack of commutation of the filters with spatial derivatives in the presence of boundaries. We compute a large-scale part of the vertical component of relative vorticity in two ways, first by filtering the velocity and then computing vorticity from the result $\nabla \times \bar{\mathbf{u}}$, and second by computing the vorticity directly from the velocity and then applying the filter to the result $\overline{\nabla \times \mathbf{u}}$. The filter is isotropic, and uses a Gaussian target with a length scale of 100 km. The data is from a state-of-

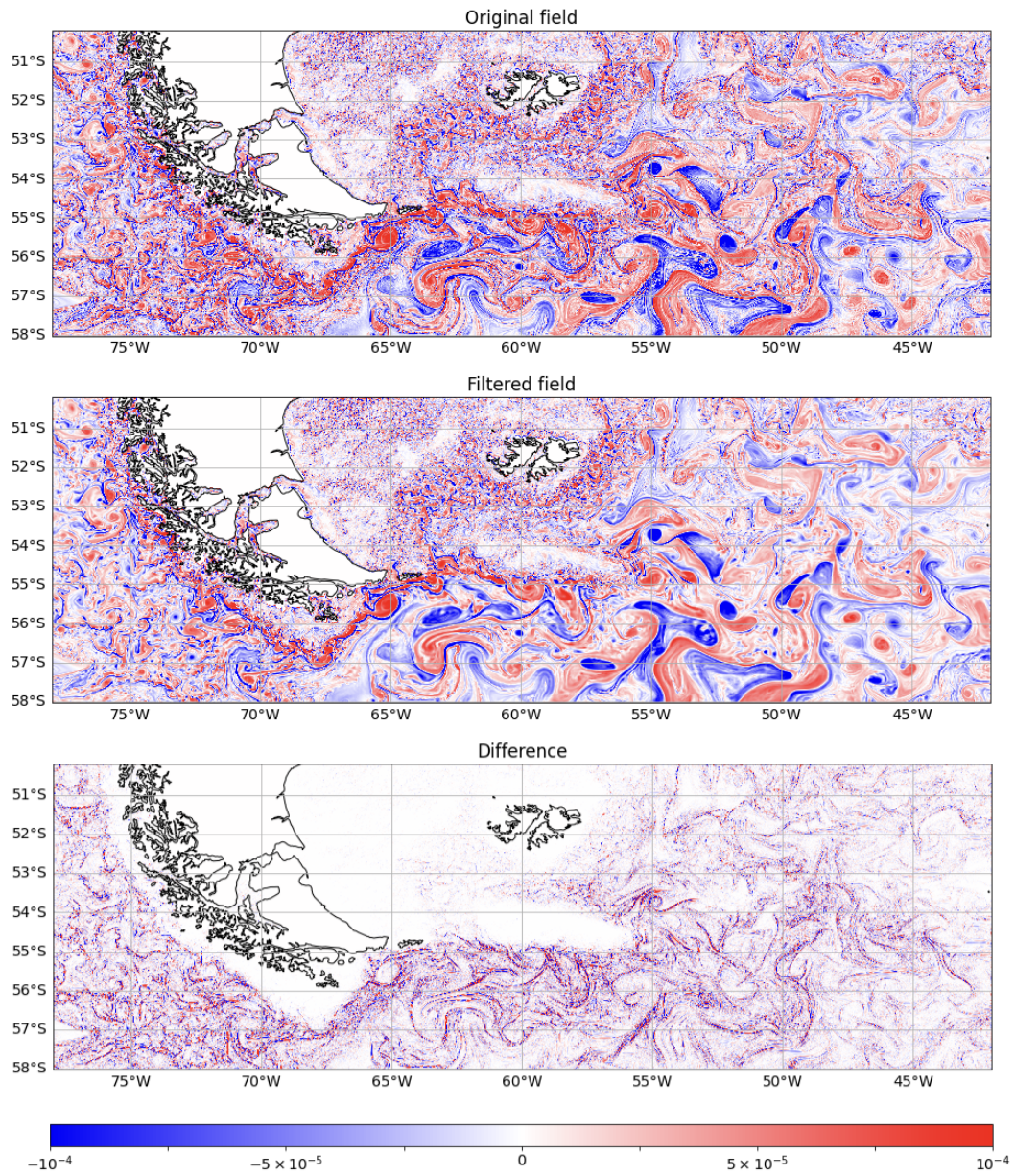


Figure 7. Surface relative vorticity from the MITgcm simulation in Bachman et al. (2017) demonstrating a spatially variable filter scale. The filter applied to the raw field (top panel) results in smoothing where the first baroclinic deformation radius is small compared to the scale of the motion (middle panel), which is reflected in the difference between the raw and filtered fields (bottom panel). Units are s^{-1} .

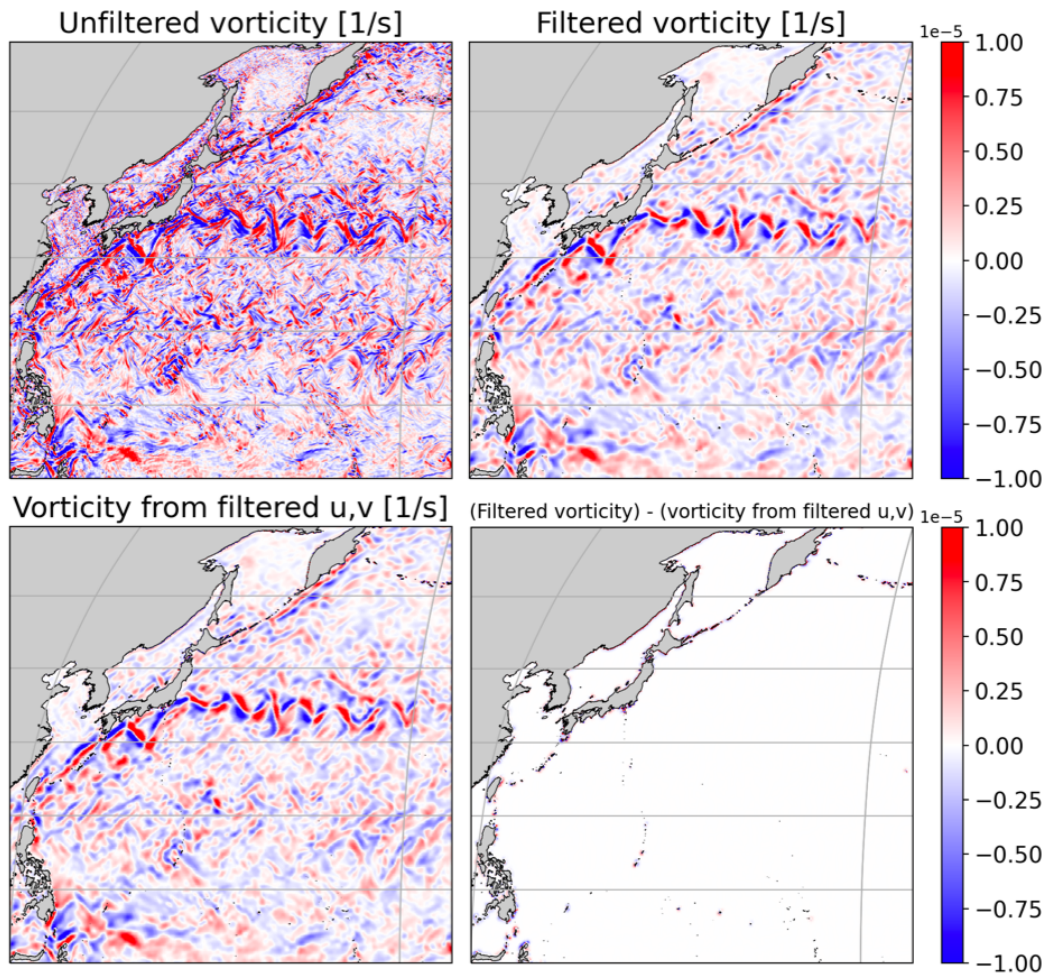


Figure 8. Surface relative vorticity fields taken from CM2.6 data. The upper left panel shows the unfiltered vorticity, the upper right shows the filtered vorticity, the bottom left panel shows the vorticity computed from filtered velocities, and the bottom right panel shows the difference between the latter two fields.

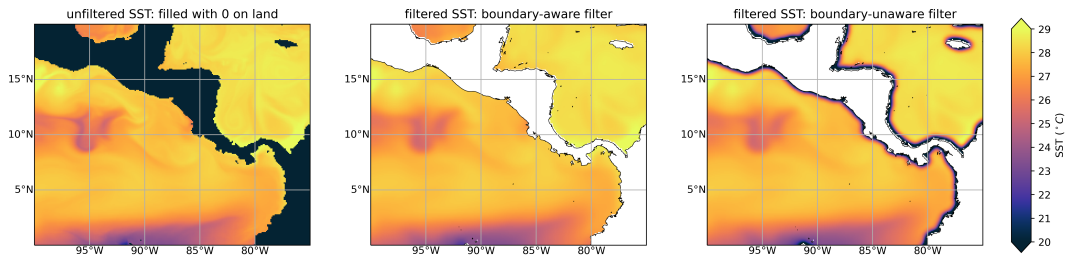


Figure 9. The left panel shows SST from a single 5-day average of the 0.1 degree resolution POP simulation in Johnson et al. (2016), with values on land set to 0. The center panel shows the simple Gaussian fixed factor filter with a filter scale 10 times the local grid scale applied to the left panel, with a no-flux condition at land boundaries. The right panel is filtered SST as in the middle panel, but ignoring land boundaries instead of using a no-flux boundary condition. Ignoring the boundaries introduces artificial bands of cold waters near the coasts. Units are degrees Celsius.

566 the-art climate model, CM2.6 (Delworth et al., 2012; Griffies, 2015), obtained through
 567 the Pangeo cloud data library (Abernathy et al., 2021). The ocean component of
 568 CM2.6 utilizes the GFDL-MOM5 numerical ocean code with a nominal resolution of
 569 0.1 degrees. The upper left panel shows the raw vorticity in the northwest Pacific,
 570 while the upper right and lower left panels show the filtered vorticity and the vorticity
 571 obtained from the filtered velocity, respectively. The lower right panel shows the
 572 difference between the two smoothed vorticities, and it is clear that the differences are
 573 extremely small over most of the domain. Significant differences arise only near the
 574 boundaries, as can be seen especially in the vicinity of the Philippines, which serves to
 575 illustrate the fact that the filter does not commute with derivatives near boundaries.

576 The ability to commute the filter with spatial derivatives can be restored by
 577 treating values on land as zero, following Aluie et al. (2018). To illustrate a potential
 578 downside of this approach we compare in Figure 9 the filtered sea surface temperature
 579 (SST) that results from the two approaches. The left panel shows the unfiltered SST,
 580 while the middle panel shows the SST filtered using the no-flux condition on the
 581 discrete Laplacian. The right panel shows the result of filtering SST over the entire
 582 domain, including land, while filling values on land with zero. The effect is to introduce
 583 bands of extremely cold water within one filter scale of the coast; in the right panel
 584 of Figure 9, SST reaches values as low as 6°C near Panama’s coasts. It is thus clear
 585 that both methods have pros and cons near boundaries. The data used in Figure 9 are
 586 from the CORE-forced POP simulation described in Johnson et al. (2016); the filter
 587 is the simple fixed factor filter of Section 2.6, with a filter scale 10 times the local grid
 588 scale and a Gaussian target.

589 3.4 Negative weights and eddy kinetic energy

590 The Gaussian filter’s effective kernel has positive weights, while the more scale-
 591 selective taper filter’s effective kernel typically has negative weights reminiscent of the
 592 sinc kernel that corresponds to the spectral truncation filter. These negative weights
 593 can produce negative values for non-negative quantities like eddy kinetic energy. We
 594 define eddy kinetic energy (EKE) as

$$\text{EKE} = \frac{1}{2} \overline{|\mathbf{u}|^2} - \frac{1}{2} |\bar{\mathbf{u}}|^2. \quad (39)$$

595 This definition of EKE has the virtue that the total kinetic energy is exactly the sum
 596 of the mean and eddy kinetic energies. When the weights are positive, it can be shown

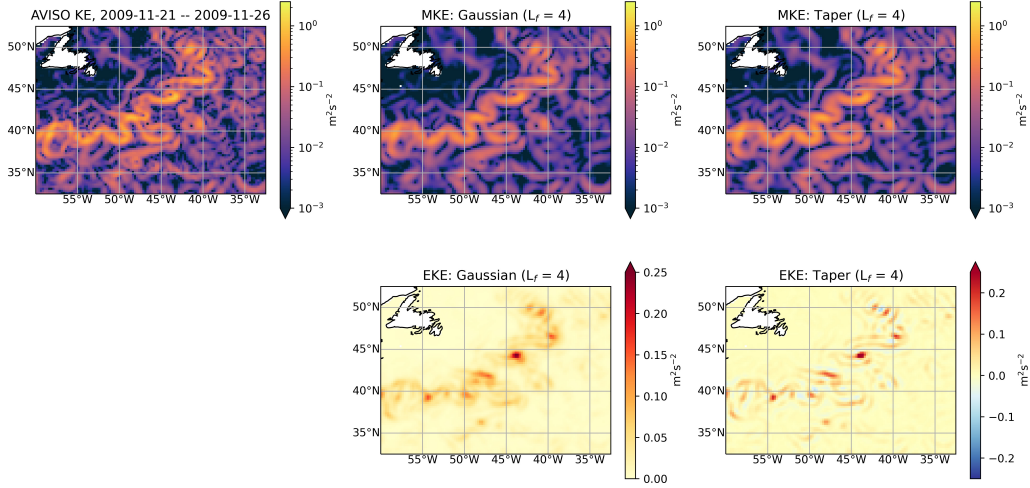


Figure 10. The left panel shows surface kinetic energy calculated from absolute geostrophic velocities estimated using AVISO measurements of sea surface height. Velocities are provided on a $1/4^\circ$ degree grid and filtered using a Gaussian (middle column) and taper (right column) simple fixed filter with filter scale 4 times the local grid scale. Definitions of mean kinetic energy (MKE) and eddy kinetic energy (EKE) are provided in the text.

597 using the Cauchy-Schwartz inequality that the definition (39) will never produce a
 598 negative EKE.

599 Figure 10 illustrates the application of our filters to a single five-day average of
 600 AVISO estimates of absolute geostrophic velocity on a 0.25° degree grid obtained from
 601 Copernicus European Earth Observation program [<https://marine.copernicus.eu>]
 602 via Pangeo (Abernathey et al., 2021). The upper left panel shows the unfiltered surface
 603 kinetic energy defined as $|\mathbf{u}|^2/2$. To compute mean surface kinetic energy we use the
 604 simple fixed factor Laplacian with a filter scale four times the local grid scale, i.e. a
 605 filter scale of 1 degree. The center panel in the upper row shows the mean kinetic
 606 energy defined as $|\bar{\mathbf{u}}|^2/2$ using a Gaussian target, while the upper right panel shows
 607 the mean kinetic energy obtained using the taper target. The lower panels show the
 608 surface eddy kinetic energy defined according to (39). It is clear that the negative
 609 weights in the taper filter lead to locally negative values of surface EKE.

610 The alternative definition $|\mathbf{u}'|^2/2$ where $\mathbf{u}' = \mathbf{u} - \bar{\mathbf{u}}$ can also produce negative
 611 values of EKE when the filter has negative weights. As a simple example consider
 612 the case where \mathbf{u}' is nonzero at only one grid point. Then $|\mathbf{u}'|^2$ is proportional to
 613 the effective kernel centered at that point, and Figure 6 shows that the taper filter's
 614 effective kernel has negative weights.

615 3.5 Application to one-dimensional observational data

616 Our final example in Figure 11 illustrates the application of our filters to one-
 617 dimensional data, specifically along-track altimeter observations of absolute dynamic
 618 topography used to estimate cross-track geostrophic velocity. This example is in-
 619 cluded not only to highlight additional capabilities of this filtering framework, but
 620 also to encourage its use on in-situ velocity or tracer measurements to permit scale-
 621 aware observational-model comparisons. We apply three filters (boxcar, Gaussian, and
 622 taper) to cross-track geostrophic velocity estimates along a single track of the Jason-2

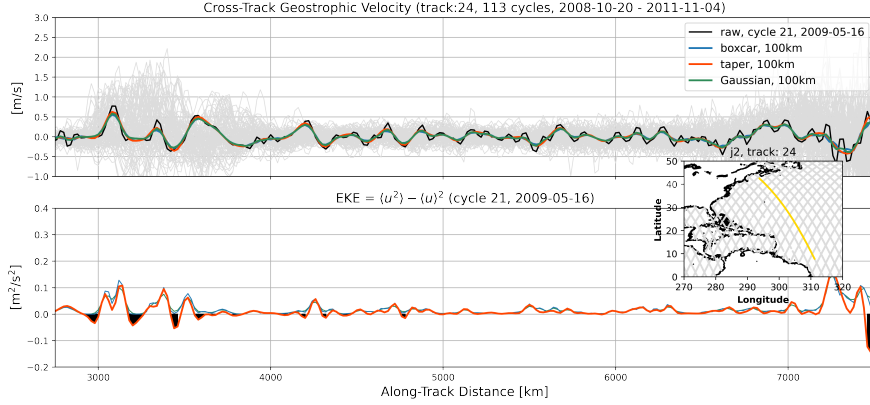


Figure 11. The upper panel shows cross-track geostrophic velocities along the Jason-2 altimeter track number 24 spanning a two-year period (grey). A single cycle is selected (black) and filtered using the boxcar (blue), taper (red), and Gaussian (green) filters using a 100 km filter scale. The inset figure locates track 24 in the Western North Atlantic with along-track distance increasing north to south. The lower panel shows eddy kinetic energy defined using the cross-track geostrophic velocities above and filtered using boxcar, taper, and Gaussian filters. Shaded black regions identify locations of negative EKE associated with the taper filter.

623 altimeter located in the Western North Atlantic. Velocities are interpolated to 20 km
 624 spacing and then filtered to a 100 km filter scale. The upper panel shows a single
 625 cycle of cross-track geostrophic velocity as a function of along-track distance moving
 626 north to south (grey lines show all cycles completed at 10 day intervals over a two year
 627 period). The single cycle (black) is then filtered using each of the three filter types
 628 with EKE shown in the lower panel. The three filters produce nearly indistinguishable
 629 large-scale fields, but the EKE defined according to equation (39), shown in the lower
 630 panel, displays notable differences. Specifically, the taper filter's negative weights lead
 631 to occasional negative values for EKE.

632 4 Conclusions

633 We have presented a new method for spatially filtering gridded data that only
 634 relies on the availability of a discrete Laplacian operator. The method involves re-
 635 peated steps of the form (21b), and is therefore analogous to smoothing via diffusion.
 636 The new filters provide an efficient way of implementing something close to a Gaussian
 637 kernel convolution; they also allow the scale selectiveness (i.e. the shape) of the filter
 638 to be tuned as desired. As they require only the ability to apply a discrete Laplacian
 639 operator, these filters can be used with a wide range of data types, including output
 640 from models on unstructured grids, and gridded observational data sets.

641 In the presence of boundaries, and when the filter scale varies over the domain, the
 642 new filters do not commute with spatial derivative. In domains without boundaries, the
 643 new filters will commute with any spatial derivative that commutes with the Laplacian,
 644 at least provided that the filter length scale does not change over the domain. If desired,
 645 ocean boundaries can be eliminated by treating values on land as zero, following Aluie
 646 et al. (2018); however, in order to preserve the integral with this method, the integral
 647 has to be extended over land. The basic method can be generalized to allow for
 648 anisotropic, i.e direction-dependent, as well as spatially-varying filter scales. It is our

649 hope that the new method and forthcoming software package will enable an increase
 650 in scale-dependent analysis of Earth system data, particularly for the purposes of
 651 subgrid-scale parameterization, though by no means limited to such.

652 Acknowledgments

653 We are grateful to J. Busecke for help with setting up the `gcm-filters` Python pack-
 654 age, and to H. Khatri for discovering the numerical instability described in section
 655 2.4. We thank A. Adcroft for helpful discussions on the design of spatially-varying
 656 filters. Scripts used to generate the figures, including links to the publicly-available
 657 data, can be found at (Loose et al., 2021). We are grateful to F. Bryan for provid-
 658 ing us with the output of the POP model simulations from (Johnson et al., 2016).
 659 A open-source python package implementing this algorithm, called `gcm-filters`, is
 660 currently under development (see (*gcm-filters*, 2021)). An early version of the package
 661 was used to generate the results in this paper. A paper describing the software itself is
 662 in preparation for Journal of Open Source Software, to coincide with the first release.
 663 In the present manuscript, our focus is the algorithm itself, not the implementation.
 664 I.G. and N.L. are supported by NSF OCE 1912332. R.A. is supported by NSF OCE
 665 1912325. J.S. is supported by NSF OCE 1912302. S.B. and G.M. are supported by
 666 NSF OCE 1912420. A.G. and E.Y. are supported by NSF GEO 1912357 and NOAA
 667 CVP NA19OAR4310364.

668 Appendix A Solving the optimization problem to find the filter poly- 669 nomial

670 We may find a polynomial that approximates the target filter by solving an
 671 optimization problem of the form

$$p(s) = \arg \min \|\hat{G}_t(\sqrt{s}) - p(s)\|, \quad (\text{A1})$$

672 where $s = k^2$ and p is a polynomial that must satisfy $p(0) = 1$. In order to enable rapid
 673 solution of this optimization problem it is convenient to use a weighted L^2 norm on
 674 $s \in [0, s_{\max}]$, where (as noted above) we may set $s_{\max} = k_{\max}^2 = (\sqrt{d}\pi/dx_{\min})^2$ where d
 675 is the dimension of the spatial domain. Using the Chebyshev norm is known to produce
 676 solutions that are close to the solution obtained from the max norm (Trefethen, 2019,
 677 theorem 16.1), so we adopt the Chebyshev norm

$$\|\hat{G}_t(\sqrt{s}) - p(s)\|_C^2 = \int_0^{s_{\max}} \frac{(\hat{G}_t(\sqrt{s}) - p(s))^2}{\sqrt{s(s - s_{\max})}} ds. \quad (\text{A2})$$

678 The polynomial must satisfy $p(0) = 1$ in order to conserve the integral, and for conve-
 679 nience we also apply the condition $p(s_{\max}) = 0$. This allows us to solve the optimization
 680 problem using the Galerkin basis described by (Shen, 1995). To be precise, we let

$$p(s) = 1 - \frac{s}{s_{\max}} + \sum_{i=0}^{N-2} \hat{p}_i \phi_i(s), \quad (\text{A3})$$

681 where $\phi_i(s)$ are the polynomial basis of Shen (1995), satisfying $\phi_i(0) = \phi_i(s_{\max}) = 0$,
 682 and $\phi_i(s)$ is a polynomial of degree $i + 2$. Collecting the Galerkin coefficients \hat{p}_i into a
 683 vector $\hat{\mathbf{p}}$, standard arguments show that the optimal polynomial coefficients are given
 684 by the solution of

$$\mathbf{M}\hat{\mathbf{p}} = \mathbf{b}, \quad (\text{A4})$$

685 where

$$M_{ij} = \langle \phi_i(s), \phi_j(s) \rangle_C \quad (\text{A5})$$

$$b_i = \langle \phi_i(s), \hat{G}_t(\sqrt{s}) - 1 - \frac{s}{s_{\max}} \rangle_C, \quad (\text{A6})$$

686 and $\langle \cdot, \cdot \rangle_C$ denotes the Chebyshev inner product. The entries of \mathbf{M} are known an-
 687 alytically (Shen, 1995), and the entries of \mathbf{b} are computed using Gauss-Chebyshev
 688 quadrature with $N + 1$ points.

689 Once a target filter $\hat{G}_t(k)$ has been specified, one must also choose the degree
 690 N of the polynomial p . As N increases the filter approaches the target filter, but at
 691 the same time the computational cost of the filter grows because applying the filter
 692 requires applying the discrete Laplacian N times. It is therefore desirable to choose
 693 some tradeoff between cost and accuracy. The Python package `gcm-filters` (*gcm-*
 694 *filters*, 2021) has a default setting for N that guarantees not more than 1% error in
 695 the difference between \hat{G}_t and p ; the user can also override this choice with any desired
 696 value of N .

697 Appendix B Commuting the filter and derivatives

698 This section explores conditions under which our filters commute with spatial
 699 derivatives, which was one of the main goals in the design of convolution-based spatial
 700 filters on the sphere in Aluie (2019). Filters with spatially-varying properties (cf.
 701 Section 2.6) do not commute with derivatives, since they are analogous to integration
 702 against a spatially-varying kernel (i.e. equation (8)). We thus consider in this section
 703 only the versions of our filters with a fixed length scale. We first consider domains
 704 with boundaries, showing that our filters do not commute in this case, and then turn
 705 to the surface of a full sphere, without topographic boundaries.

706 Although our filters are defined entirely in discrete terms, it is natural to think in
 707 terms of the continuous limit, and this limit causes confusion. Consider for simplicity
 708 the case of the following filter for a scalar function $f(x)$ on $x \in [0, 1]$:

$$\bar{f} = \left(1 - \frac{1}{s_1} \Delta\right) f. \quad (\text{B1})$$

709 This filter obviously commutes with derivatives, but it is in some sense not the correct
 710 continuous version of our discrete filter. The reason is that the discrete version always
 711 assumes no-flux boundary conditions on the data, because no other boundary condition
 712 is guaranteed to conserve the integral. Indeed the filter (B1) is not guaranteed to
 713 conserve the integral unless f satisfies no-flux (or periodic) boundary conditions. This
 714 is no limitation in the discrete case, since the no-flux Laplacian can be computed for
 715 any data. On the other hand, if one applies the discrete Laplacian with a no-flux
 716 assumption and then takes the limit of infinite resolution the result does not converge
 717 to Δf unless f actually satisfies no-flux boundary conditions. Instead, it converges
 718 to Δf plus Dirac delta distributions on the boundary. (This is analogous to the delta
 719 sheets of potential vorticity discussed by Bretherton (1966).)

720 In the correct continuous limit, equation (B1) is only defined for functions f that
 721 satisfy $f'(0) = f'(1) = 0$. With this more careful definition of the continuous limit of
 722 the filter, one can ask again whether it commutes with the spatial derivative. If one
 723 attempts to define $g(x) = f'(x)$ and then apply the filter to g , the result is not defined
 724 unless g also satisfies no-flux conditions, i.e. $f''(0) = f''(1) = 0$. So in the continuous
 725 limit, the filter will not commute with differentiation for functions with $f'' \neq 0$
 726 on the boundaries. For higher-order filters the conditions for commutation are even more
 727 stringent, requiring derivatives up to high order to all be zero on the boundary.

728 An alternative perspective is afforded by the fact that our discrete filter is equiv-
 729 alent to a discrete kernel smoothing, per the arguments of Section 2.8. In the presence
 730 of boundaries, the shape of the kernel varies in space, as can be seen in Figure 6.
 731 The continuous analog is integration against a spatially-varying kernel (equation (8)),
 732 which does not commute with spatial derivatives.

733 In the case without boundaries, e.g. on a sphere, there is no such difficulty. As
 734 long as the continuous differential operators commute (e.g. a Laplacian and a gradi-
 735 ent), the discrete operators should also commute, at least up to discretization errors.
 736 The convolution-based spatial filters of Aluie (2019) only commute with derivatives in
 737 the absence of boundaries; this difficulty can be avoided by treating values outside the
 738 domain (e.g. on land) as zero (Aluie et al., 2018). A similar method can be used with
 739 our filters if desired: values outside the domain can be treated as zero (see right panel
 740 of Figure 9). The development in Section 2.3 is based on a discrete approximation of
 741 a scalar Laplacian, or of the Laplace-Beltrami operator on a curved surface like the
 742 sphere. This can in principle be extended to vector Laplacians, for example if one
 743 wants a filter that commutes the filtering operation on a vector field with divergence
 744 or curl of the field, by simply replacing \mathbf{L} with a discretization of the vector Laplacian.

745 References

- 746 Abernathey, R., Augspurger, T., Banihirwe, A., Blackmon-Luca, C., Crone, T., Gen-
 747 temann, C., ... Signell, R. (2021). Cloud-native repositories for big scientific
 748 data. *Computing in Science and Engineering*(01), 1–1.
- 749 Aluie, H. (2019). Convolutions on the sphere: commutation with differential opera-
 750 tors. *GEM-International Journal on Geomathematics*, 10(1), 9.
- 751 Aluie, H., Hecht, M., & Vallis, G. K. (2018). Mapping the energy cascade in the
 752 North Atlantic Ocean: The coarse-graining approach. *J. Phys. Ocean.*, 48(2),
 753 225–244.
- 754 Bachman, S. D., Taylor, J., Adams, K., & Hosegood, P. (2017). Mesoscale
 755 and submesoscale effects on mixed layer depth in the Southern Ocean.
 756 *J. Phys. Ocean.*, 47(9), 2173–2188.
- 757 Báez Vidal, A., Lehmkuhl, O., Trias, F. X., & Pérez-Segarra, C. D. (2016). On the
 758 properties of discrete spatial filters for CFD. *J. Comput. Phys.*, 326, 474–498.
- 759 Berloff, P. S. (2005). On dynamically consistent eddy fluxes. *Dyn. Atmos. Oceans*,
 760 38(3-4), 123–146.
- 761 Berloff, P. S. (2018). Dynamically consistent parameterization of mesoscale eddies.
 762 Part III: Deterministic approach. *Ocean Model.*, 127, 1–15.
- 763 Bolton, T., & Zanna, L. (2019). Applications of deep learning to ocean data in-
 764 ference and subgrid parameterization. *J. Adv. Model. Earth Syst.*, 11(1), 376–
 765 399.
- 766 Bretherton, F. (1966). Critical layer instability in baroclinic flows. *Q. J. Roy. Me-
 767 teor. Soc.*, 92(393), 325–334.
- 768 Delworth, T., Rosati, A., Anderson, W., Adcroft, A., Balaji, V., Benson, R., ...
 769 R, Z. (2012). Simulated climate and climate change in the GFDL CM2.5
 770 high-resolution coupled climate model. *J. Climate*, 25(8), 2755–2781.
- 771 *gcm-filters*. (2021). <https://github.com/ocean-eddy-cpt/gcm-filters>. (Ac-
 772 cessed: 2021-03-24)
- 773 Germano, M. (1986). Differential filters for the large eddy numerical simulation of
 774 turbulent flows. *Phys. Fluids*, 29(6), 1755–1757.
- 775 Griffies, S. M. (2015). A handbook for the GFDL CM2-0 model suite. *GFDL Cli-
 776 mate Processes and Sensitivity Group, Technical Report #1*.
- 777 Grooms, I., & Kleiber, W. (2019). Diagnosing, modeling, and testing a multiplica-
 778 tive stochastic Gent-McWilliams parameterization. *Ocean Model.*, 133, 1–10.
- 779 Grooms, I., Nadeau, L.-P., & Smith, K. S. (2013). Mesoscale eddy energy locality in
 780 an idealized ocean model. *J. Phys. Ocean.*, 43, 1911–1923.
- 781 Guedot, L., Lartigue, G., & Moureau, V. (2015). Design of implicit high-order filters
 782 on unstructured grids for the identification of large-scale features in large-eddy
 783 simulation and application to a swirl burner. *Phys. Fluids*, 27(4), 045107.
- 784 Guillaumin, A., & Zanna, L. (2021). Stochastic deep learning parameterization of
 785 ocean momentum forcing. *Earth and Space Science Open Archive*, 31. doi: 10

- 786 .1002/essoar.10506419.1
- 787 Haigh, M., Sun, L., Shevchenko, I., & Berloff, P. (2020). Tracer-based estimates of
- 788 eddy-induced diffusivities. *Deep-sea Res. Pt. I*, 103264. doi: 10.1016/j.dsr.2020
- 789 .103264
- 790 Hunter, J. K., & Nachtergaele, B. (2001). *Applied analysis*. World Scientific.
- 791 Johnson, B. K., Bryan, F. O., Grodsky, S. A., & Carton, J. A. (2016). Clima-
- 792 tological annual cycle of the salinity budgets of the subtropical maxima.
- 793 *J. Phys. Ocean.*, 46(10), 2981–2994.
- 794 Khani, S., Jansen, M. F., & Adcroft, A. (2019). Diagnosing subgrid mesoscale eddy
- 795 fluxes with and without topography. *J. Adv. Model. Earth Syst.*.
- 796 Loose, N., Grooms, I., Busecke, J., & Yankovsky, E. (2021, March). *ocean-eddy-*
- 797 *cpt/gcm-filters-paper: Diffusion-based smoothers for spatial filtering of gridded*
- 798 *geophysical data*. Zenodo. doi: 10.5281/zenodo.4633794
- 799 Lu, J., Wang, F., Liu, H., & Lin, P. (2016). Stationary mesoscale eddies, upgradient
- 800 eddy fluxes, and the anisotropy of eddy diffusivity. *Geo. Res. Lett.*, 43(2), 743–
- 801 751.
- 802 Nadiga, B. (2008). Orientation of eddy fluxes in geostrophic turbulence.
- 803 *Phil. Trans. R. Soc. A*, 366(1875), 2489–2508.
- 804 Porta Mana, P., & Zanna, L. (2014). Toward a stochastic parameterization of ocean
- 805 mesoscale eddies. *Ocean Model.*, 79, 1–20.
- 806 Raymond, W. H. (1988). High-order low-pass implicit tangent filters for use in finite
- 807 area calculations. *Mon. Weather Rev.*, 116(11), 2132–2141.
- 808 Raymond, W. H., & Garder, A. (1991). A review of recursive and implicit filters.
- 809 *Mon. Weather Rev.*, 119(2), 477–495.
- 810 Robinson, G., & Grooms, I. (2020). A fast tunable blurring algorithm for scattered
- 811 data. *SIAM J. Sci. Comput.*, 42(4), A2281–A2299.
- 812 Ryzhov, E., Kondrashov, D., Agarwal, N., & Berloff, P. (2019). On data-driven
- 813 augmentation of low-resolution ocean model dynamics. *Ocean Model.*, 142,
- 814 101464.
- 815 Sadek, M., & Aluie, H. (2018). Extracting the spectrum of a flow by spatial filtering.
- 816 *Phys. Rev. Fluids*, 3(12), 124610.
- 817 Sagaut, P., & Grohens, R. (1999). Discrete filters for large eddy simulation. *Int. J.*
- 818 *Numer. Meth. Fl.*, 31(8), 1195–1220.
- 819 Shapiro, R. (1970). Smoothing, filtering, and boundary effects. *Rev. Geophys.*, 8(2),
- 820 359–387.
- 821 Shen, J. (1995). Efficient spectral-Galerkin method II. Direct solvers of second-and
- 822 fourth-order equations using Chebyshev polynomials. *SIAM J. Sci. Comput.*,
- 823 16(1), 74–87.
- 824 Smith, R., Jones, P., Briegleb, B., Bryan, F., Danabasoglu, G., Dennis, J., . . . others
- 825 (2010). The parallel ocean program (POP) reference manual. *Los Alamos*
- 826 *National Lab Technical Report*, 141.
- 827 Stanley, Z., Bachman, S., & Grooms, I. (2020). Vertical structure of ocean
- 828 mesoscale eddies with implications for parameterizations of tracer transport.
- 829 *J. Adv. Model. Earth Syst.*, 12(10), e2020MS002151.
- 830 Stanley, Z., Grooms, I., Kleiber, W., Bachman, S., Castruccio, F., & Adcroft, A.
- 831 (2020). Parameterizing the impact of unresolved temperature variability on the
- 832 large-scale density field: Part 1. Theory. *J. Adv. Model. Earth Syst.*, 12(12),
- 833 e2020MS002185.
- 834 Trefethen, L. (2019). *Approximation theory and approximation practice, extended*
- 835 *edition*. SIAM, Philadelphia, USA.
- 836 Williams, P., Howe, N., Gregory, J., Smith, R., & Joshi, M. (2016). Improved cli-
- 837 mate simulations through a stochastic parameterization of ocean eddies. *J. Cli-*
- 838 *mate*, 29, 8763–8781.
- 839 Zanna, L., & Bolton, T. (2020). Data-driven equation discovery of ocean mesoscale
- 840 closures. *Geo. Res. Lett.*, 47(17), e2020GL088376.